

Study of Trip-Induced Hypersonic Boundary Layer Transition

Prakash Shrestha*, Joseph W. Nichols[†] and Graham V. Candler[‡]

University of Minnesota, Minneapolis, MN, 55455, USA

Mihailo R. Jovanović[§]

University of Southern California, Los Angeles, CA, 90007, USA

We study the transition of a Mach 5.65 laminar boundary layer tripped by an array of diamond shaped roughness elements using large-scale direct numerical simulations. A low Reynolds number experiment conducted at the Actively Controlled Expansion Hypersonic Wind Tunnel, Texas A & M University National Aerothermochemistry Laboratory is used to validate our simulation. Planar acoustic disturbances are applied at the inflow boundary to mimic the wind tunnel ambient environment. To accurately capture flow physics, a high-order, low-dissipation scheme for the convection terms in the Navier-Stokes equations is used. Visualizations and statistics of the flow explore the dominant and dynamically significant flow structures : the upstream vortex system, the shock system, and the downstream separated shear layer/wake region which originates from the top and sides of the roughness elements. Three-dimensional snapshots of pressure were considered to select dominant dynamic mode decomposition modes using Chu's disturbance energy norm. A coupled system at 30 kHz consisting of the shock system, the separated shear layer/wake region and the upstream vortex system is determined to have the most disturbance energy. The origin of disturbances is observed to be the upstream vortex system while the wake region acts as a dominant amplifier. Comparison of the flow structures and modes of transition between an isolated cylindrical roughness element and the array of diamond shaped roughness elements is performed.

Nomenclature

FFT	Fast fourier transformation
DMD	Dynamic mode decomposition
Re_θ	Reynolds number based on momentum thickness
D	Diagonal length of a trip cross-section parallel to the wall = 3.18 mm
k	Roughness height = 4.76 mm
δ	Unperturbed boundary layer thickness at a trip location = 3.2 mm.
s	Trip spacing = 6.36 mm
α_{DMD}	Amplitude of a DMD mode
λ	Complex eigenvalue of a DMD mode

I. Introduction

Surface roughness enhances laminar-to-turbulent transition processes in both low- and high speed boundary layers. Therefore, predicting whether the flow over a given roughness distribution will remain laminar or

*Graduate Research Assistant, Aerospace Engineering and Mechanics, AIAA Student Member.

[†]Assistant Professor, Aerospace Engineering and Mechanics, AIAA Member.

[‡]Russell J. Penrose and McKnight Presidential Professor, Aerospace Engineering and Mechanics, AIAA Fellow.

[§]Professor, Electrical Engineering-Systems, IEEE Senior Member.

become turbulent may be a vital design and safety issue. Furthermore, the dominant transition mechanism in the boundary layers can be significantly altered using roughness elements by accelerating the transition region both in quiet and noisy environments.¹ Numerous numerical and experimental investigations have been carried out to understand trip-induced boundary layer transitions. But underlying physical mechanisms still remain incompletely explained.

One of the earliest experiments in high-speed transition is by Whitehead.² He studied flowfield and drag characteristics of several tripping-element shapes at a free-stream Mach number of 6.8 with $k/\delta = 2$. The experiment was conducted in two parts : (1) using different isolated roughness elements and (2) using an array of hemispherical roughness elements. The upstream vortex region was different for different shapes of isolated roughness elements. In case of the array of the hemispherical roughness elements (diameter (D) is constant), different trip spacings (s) yielded various flowfields upstream and downstream of the trips. In case of $s/D = 3$ and 4, the flowfield around the hemispherical roughness elements was not significantly influenced by neighboring roughness elements. However, as the s/D ratio was decreased to 2, an interaction of the flowfield between adjoining elements became more significant and the transition region was observed earlier. This means a decreasing value of the s/D ratio stagnates more fluids upstream of these elements and, therefore, alters flow physics that leads to different transition mechanisms. However, a clear explanation of the transition mechanisms was not provided by Whitehead.²

Subbareddy et al.⁶ conducted a direct numerical simulation of an isolated cylindrical roughness element at three different Reynolds numbers (low, medium and high, say) based on variable freestream densities, a fixed roughness height and freestream velocity (Mach 6). In the low Reynolds number case, no transition occurs. Quasi-turbulence was reported in the medium Reynolds number case. However, in the high Reynolds case, transition-turbulence occurs just downstream of the roughness element. This indicated that Reynolds number plays a significant role in altering flowfields downstream of the element. Furthermore, the total number of mean recirculating vortices upstream of the element increased with the increment in Reynolds number. To understand the transition mechanisms in case of high Reynolds number case, the authors used dynamic mode decomposition (DMD) to determine the most energetic modes using snapshots of pressure in a plane parallel to and at a trip height away from the wall. For detailed information on DMD, readers are referred to Schmid.⁷ Three of the most energetic DMD modes were studied. The first two modes were harmonic and sub-harmonic modes, and were related to horseshoe vortices indicating that the dominant mechanisms could be due to the horseshoe vortex system. The third mode was observed to be related to the separated shear layer region downstream of the roughness element, indicating that the second most dominant mode of transition is a pair of counter-rotating vortices from the top and the sides of the element. Furthermore, a persistent shock-system was observed in all modes indicating that pressure waves from the top upstream portion of the element could play a role in the transition mechanism. It is important to note that these modes are connected to these different mechanisms based on the intensity and location of their modal shapes.

Semper and Bowersox⁹ performed experiments to quantify flow structures in a hypersonic ($M = 5.65$) low-Reynolds number ($Re_\theta = 3600$) tripped boundary layer. An array of three-dimensional diamond-shaped trips was considered for tripping the boundary layer. The process of transition to turbulence downstream of the array was studied. A spectral peak near 58 kHz was observed in all streamwise locations at the fixed spanwise location downstream of the array. This frequency corresponded to the vortex shedding and, therefore, indicated that a Kelvin-Helmholtz type instability led to the transition process. The present work aims to investigate the source and the regions of amplification of dominant disturbances in the hypersonic boundary layer using numerical simulations. We conduct spatio-temporal analysis by DMD⁷ and FFT at different regions to understand transition mechanisms. Chu's disturbance energy norm is applied to select DMD modes based on their disturbance energy. This selection is similar to a recently developed sparsity-variant of DMD named as a sparsity-promoting DMD (SPDMD) to select the most significant DMD modes.

The paper is set-up as follows : §II describes the numerical and physical modeling, §III discusses the results of the simulations including dynamic mode decomposition and §IV concludes the present study.

II. Numerical and physical modeling

We solve the unsteady and non-reacting compressible Navier-Stokes equations for air as a calorically perfect gas in conservative form.

$$\frac{\partial U}{\partial t} + \frac{\partial F_j}{\partial x_j} = \frac{\partial F_j^v}{\partial x_j}$$

where the vector of conserved variables U is

$$U = \begin{bmatrix} \rho \\ \rho u_i \\ E \end{bmatrix}. \quad (1)$$

The convective F_j and viscous fluxes F_j^v are shown below,

$$F_j = \begin{bmatrix} \rho u_j \\ \rho u_i u_j + p \delta_{ij} \\ (E + p)u_j \end{bmatrix} \quad (2)$$

$$F_j^v = \begin{bmatrix} 0 \\ \sigma_{ij} \\ \sigma_{ij} u_i - q_{ij} \end{bmatrix} \quad (3)$$

In these equations, u_i is the i^{th} component of velocity, p is the pressure, and $E = \rho C_v T + \frac{1}{2} \rho u_i u_i$ is the total energy. The strain rate tensor σ_{ij} and the heat flux vector q_j are given by $\sigma_{ij} = 2\mu S_{ij} - \frac{2}{3}\mu S_{kk}\delta_{ij}$ and $q_j = -k \frac{\partial T}{\partial x_j}$ respectively where, S_{ij} is the symmetric part of the velocity gradient tensor. The ideal gas equation of state $p = \rho RT$ is applied. Molecular viscosity μ is calculated using Sutherland's law, $\mu = a \frac{T^{1.5}}{T+b}$ with $a = 1.458 \times 10^{-6}$ and $b = 110.4$. The thermal conductivity $k = \mu \frac{C_p}{Pr}$ is computed using a constant Prandtl number $Pr = 0.72$ and the ratio of specific heats, $\gamma = 1.4$.

For the inviscid flux computation, we use a stable, low-dissipation scheme based on the kinetic-energy consistent (KEC) method developed by Subbareddy and Candler.¹³ In this method, the inviscid flux is split into symmetric (non-dissipative) and upwind (dissipative) portions. The flux is pre-multiplied by a shock-detecting switch,¹⁴ ensuring that the dissipation occurs only at shocks. The sixth-order accurate central KEC scheme is used for our present study to maintain low dissipation and the viscous fluxes are computed using second order centered differences. Time integration is achieved using a second-order, implicit Euler method with point relaxation to maintain numerical stability and accuracy. The implicit system is solved with the data parallel line relaxation (DPLR) method.¹⁵

A. ACE wind tunnel facility

Our simulations have been performed in conjunction with an experimental campaign. The experimental facility is shown in Figure 1. The Actively Controlled Expansion Hypersonic wind tunnel¹³ is a hypersonic blow-down wind tunnel located at Texas A & M University-College Station. The length, height and width of the test section are 507, 230 and 360 mm respectively. Uniform Mach numbers (to within 1%) over a range of 5.0-7.0 are produced using a variable Mach number mechanism along with a range of Re from 0.7 - 7.0 million/meter. The run time of the facility is 40 sec.

The experiment is conducted on a 7.62-mm thick flat plate (508-mm long and 356-mm wide) with a 1.59 mm radius blunt leading edge. A 10-degree ramp is machined on the underside of the model. The leading edge of the model was positioned along the vertical centerline of the tunnel. The plate is aligned with a -2 degrees angle of attack to promote favorable pressure gradients near its leading edge. A schematic of the flat plate in the experimental facility is shown in Figure 2. Additionally, the geometry of trips is shown in Figure 3. For more details about the experimental facility, the reader is referred to Semper et al.⁹

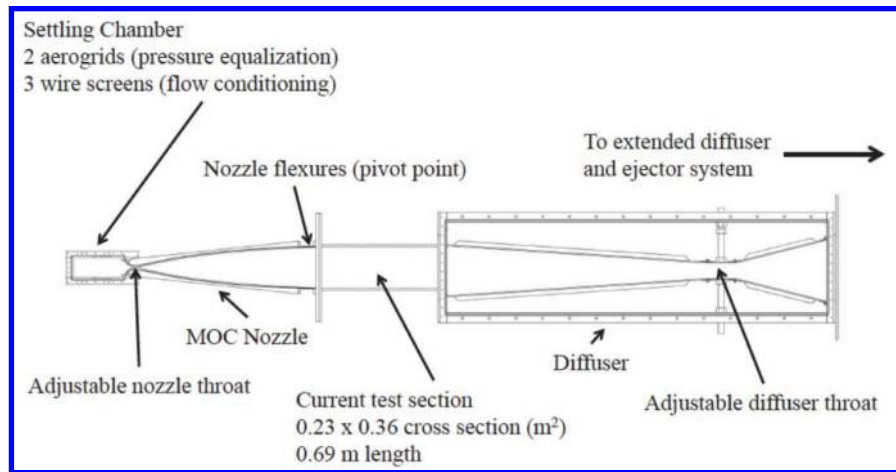


FIGURE 1: Schematic of the ACE wind tunnel flow path. Reproduced from Semper et al.⁹ with permission.

B. Flow configuration for simulations

We model the flow in the ACE wind tunnel starting at the leading edge of the plate. For computational efficiency, we first perform a 2-D simulation over a flat plate that extends 60 mm from the leading edge of the flat plate. Grid tailoring was performed to more accurately capture the leading edge shock. Second, we perform a 3-D simulation using a spanwise array of two diamond shaped roughness elements. In the experiment, there are forty seven elements. To reduce computational costs, we implement only two trips. The use of the two trips can also capture spanwise harmonic and subharmonic frequency modes. The 3-D domain extends from 30 mm to 477 mm relative to the leading edge of the flat plate. A schematic of the boundary conditions for the 3D simulation is shown in Figure 4. The freestream flow conditions are shown in Table 1.

TABLE 1: Freestream Flow Conditions

M	$P_0(KPa)$	$T_0(K)$	Re/m (m^{-1})	$(\rho u)_{rms}/(\rho u)(\%)$
5.92	448	425	4.6E6	0.5

The characterization of inlet free-stream disturbances is considered in our calculation and plays a critical role in transition in experimental facilities. Of the three possible disturbance modes (acoustic, entropy and vorticity), the acoustic mode which originates from the turbulent boundary layer on the nozzle walls is dominant.¹² Freestream disturbances are thus approximated as flow parallel and acoustic, and the pressure is assumed to have the following spectral form to satisfy the dispersion relation,

$$p' = \sum_{k=-N}^{k=N} p'_k e^{i(\alpha_k^\pm)x - w_k t} \quad (4)$$

$$\alpha_k^\pm = \frac{w_k}{U_0 \pm a_o} \quad (5)$$

where, p' is the time-dependent pressure fluctuation, p'_k is the complex frequency content of the k^{th} frequency, α_k^\pm are the fast- and slow-moving wavenumbers, w_k is the angular frequency, x is the direction of the disturbance, t is time, U_0 is the base freestream velocity, and a_o is the base speed of sound. In our case, only

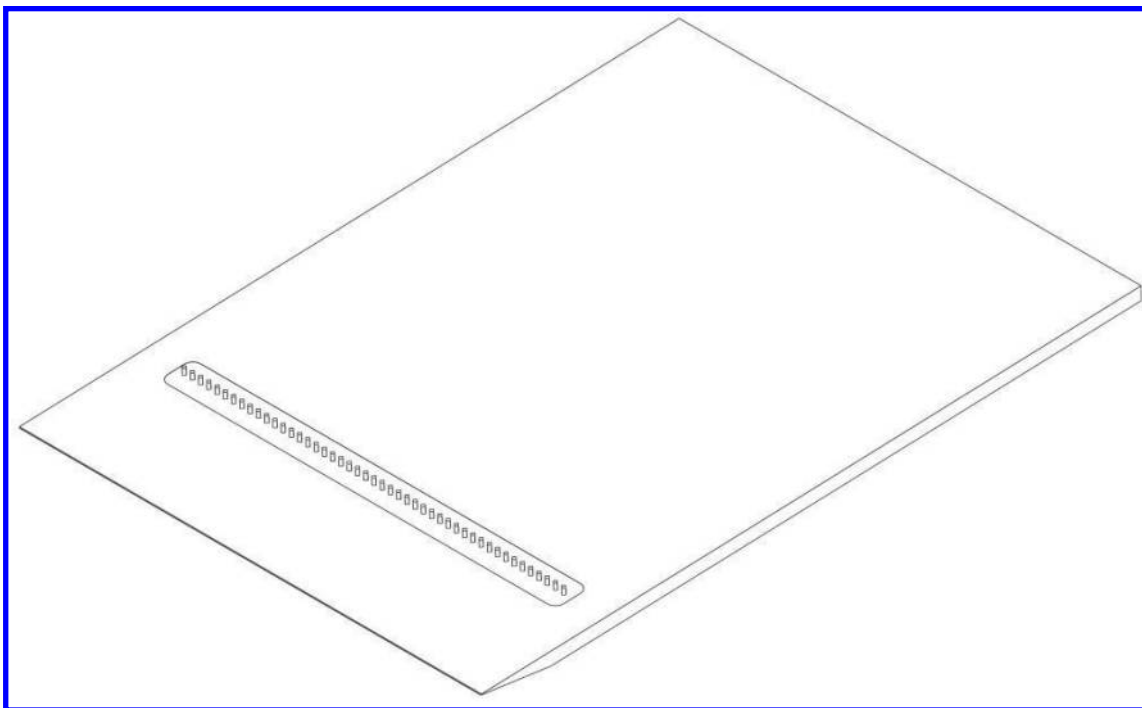


FIGURE 2: Schematic of the flat plate with the trip array. Reproduced from Semper et al.⁹ with permission.

fast-moving waves are considered. Using the linearized Euler equations, we obtain the following relations :

$$\begin{bmatrix} \rho'_k \\ u'_k \\ T'_k \end{bmatrix} = \begin{bmatrix} \frac{1}{\alpha_o^2} \\ -\frac{\alpha^\pm}{\rho_o(\alpha^\pm U_o - w_k)} \\ \frac{(\gamma-1)T_o}{\rho_o a_o^2} \end{bmatrix} p'_k \quad (6)$$

We can represent the pressure fluctuations in Fourier coefficients as :

$$p' = \sum_{k=1}^{k=N} 2|p'_k| \cos(\alpha_k^\pm x - w_k t + \phi_{p,k}) \quad (7)$$

$$|p'_k| = \sqrt{\text{Real}(p'_k)^2 + \text{Imaginary}(p'_k)^2} \quad (8)$$

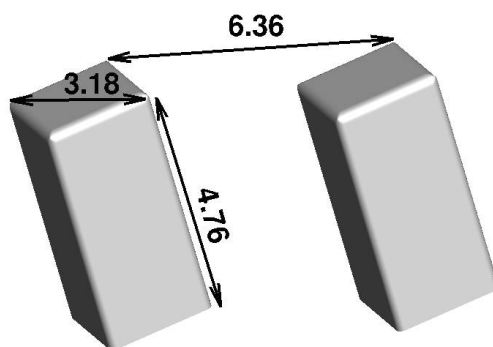


FIGURE 3: Trip Geometry. (mm)

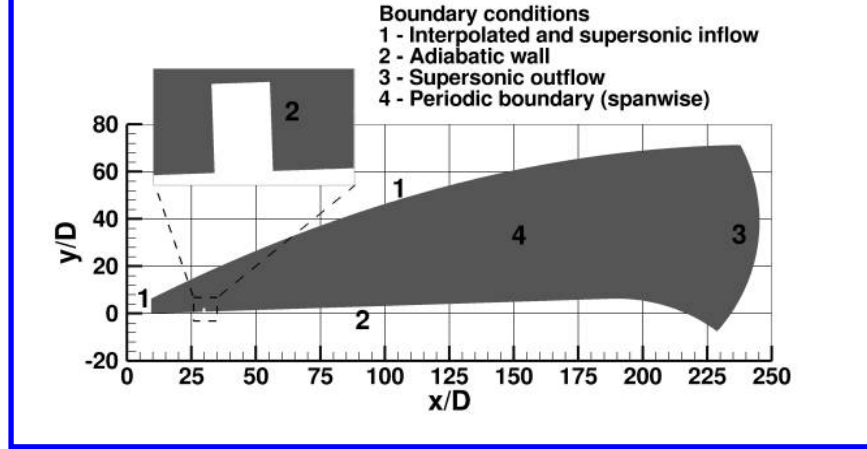


FIGURE 4: Boundary conditions for the 3-D domain.

$$\phi_{p,k} = \tan^{-1} \left(\frac{\text{Real}(p'_k)}{\text{Imaginary}(p'_k)} \right) \quad (9)$$

In the above equations, $2|p'_k|$ is the amplitude and $\phi_{p,k}$ is the phase of the k^{th} frequency component of pressure. Thus, the inflow profile is characterized using the pressure amplitude spectrum. $\phi_{p,k}$ is random between 0 and 2π to prevent superposition of peaks of different frequency modes. Furthermore, we filter the given PSD data from the facility using an interval of 2 kHz from 2 kHz to 250 kHz for our freestream $Re/m = 4.6 \times 10^6$ and Mach number = 5.92 so as to resolve frequencies accurately. We chose 2 kHz as a frequency spacing because the spacing is optimal in terms of computational time to resolve the frequency with the largest time period and retaining details of the actual inflow PSD data. The inflow freestream disturbance is shown in Figure 5. Furthermore, spikes in the spectrum are due to noise generated by the probes and resonance with the tunnel wall. We assume spikes above 80 kHz do not play significant roles in flow dynamics in our case and, therefore, are filtered out.

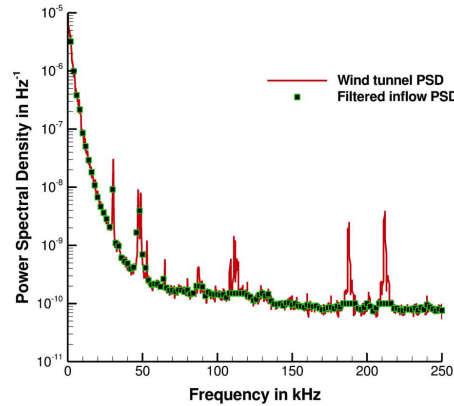


FIGURE 5: Filtering of the experimental freestream disturbances.

C. Grid generation

The converged 2-D domain contains 1 million cells and a converged 3-D domain with two trips contains 90 million cells. y^+ for both the 2-D and the 3-D domains is 0.5 near the wall. Images of the grid for the 3D flow domain near the trip are shown in Figure 6.

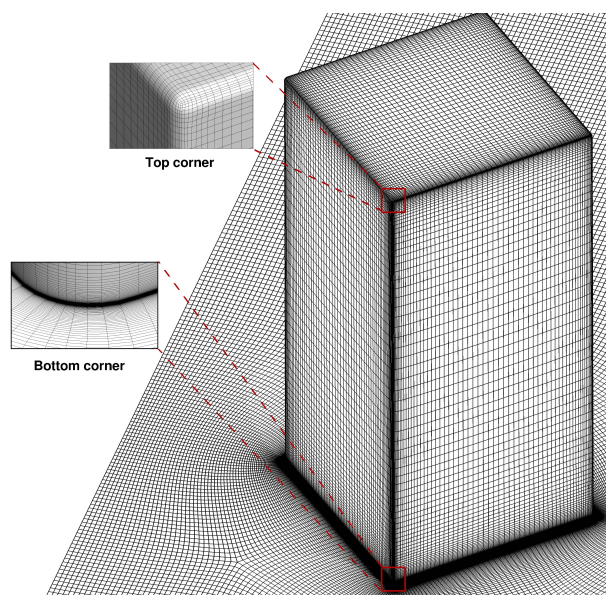


FIGURE 6: 3-D surface mesh near the trip.

III. Results

A. Three-dimensional simulation of the base domain

Analysis of three-dimensional simulations consists of three parts ; (1) comparison with the experiment, (2) study of regions of unsteadiness, and (3) spectral and modal decomposition. Length is non-dimensionalized using the trip diagonal length ($D = 3.18$ mm) and the center of the trip being $x/D = 0$. Field variables are normalized by the freestream values. Figure 7 shows grid convergence studies performed using mean streamwise mass fluxes and mean spanwise wall shear stress in two domains with 25 and 50 million cells. For the grid convergence study, the two domains extend only up to the half of the length of the flat plate for computational efficiency. At all streamwise locations, wall-normal profiles of the streamwise mass flux and spanwise profiles of the spanwise wall shear of the two domains are grid converged with minor differences.

1. Comparison with experiment

The present study is validated by comparing mean data of the numerical simulation to corresponding experimental information. Mean data is compared at $x/D = 86$ where the flow is fully developed.

In Figure 8(a), two plots of van-Driest-transformed mean velocity profile¹⁶ with respect to y^+ at $x/D = 86$ are presented. No data were available to compare the simulation in the viscous sublayer and the outer layer as shown in Figure 8a. So, comparison is carried out in the buffer and the log-law regions. In the buffer region, we observe a good agreement for larger y^+ values while, in the log-law region, there is a close agreement in all y^+ values. A possible reason of a lesser agreement at low y^+ values in the buffer layer could be the two roughness elements considered in the present study are not able to accurately capture the mean van Driest profile near the wall as compared to the profile recorded in the experiment using the forty seven roughness elements. In Figure 8(b), two plots of mean Mach number at $x/D = 86$ with respect to non-dimensionalized wall normal distance are presented. Within 5% error bars, the mean Mach profile from the DNS agree with the experimental data.

2. Study of regions of unsteadiness

This section discusses and characterizes different regions of unsteadiness. Dynamically important flow structures in the present study are : (a) the upstream vortex system, (b) the shear layer and the associated counter-rotating vortices which originate from the diamond surface and the near wake region, and (c) the shock system ahead of the roughness element. It is important to note that the domain considered from

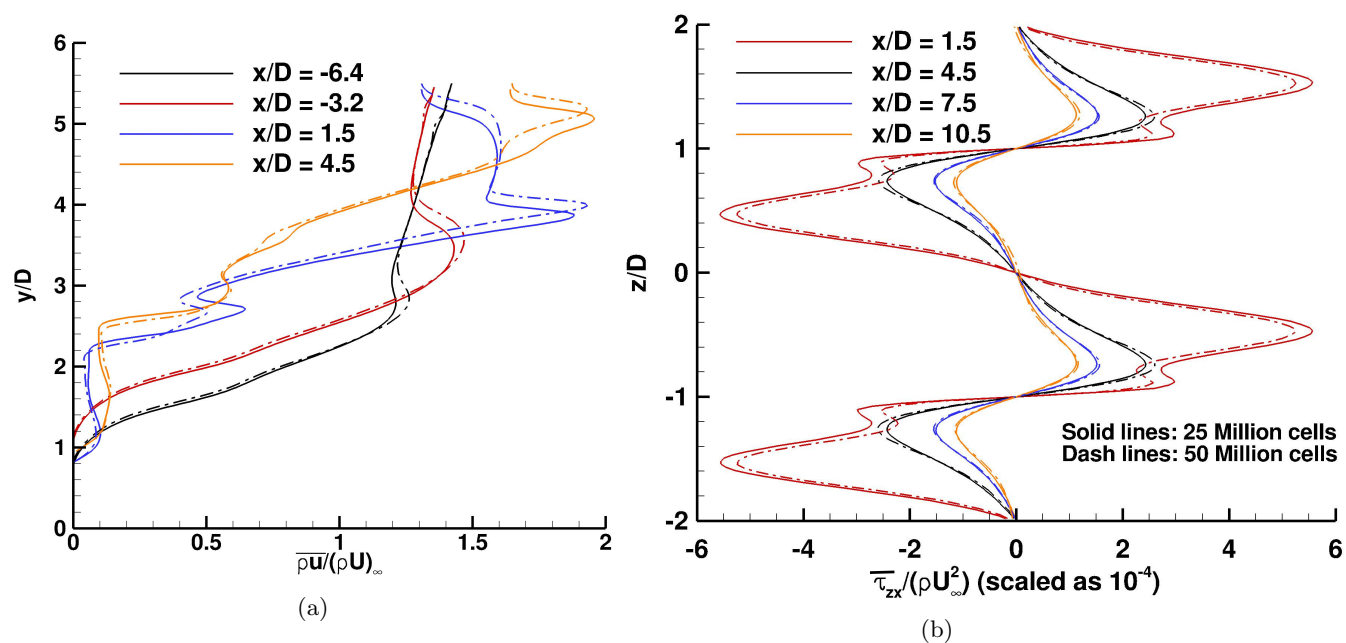


FIGURE 7: Grid convergence study using non-dimensionalized (a) mean streamwise mass flux along the wall normal direction and (b) mean wall spanwise shear stress. Solid lines :25 million cells and dash lines :50 million cells. Truncated meshes are used for the study.

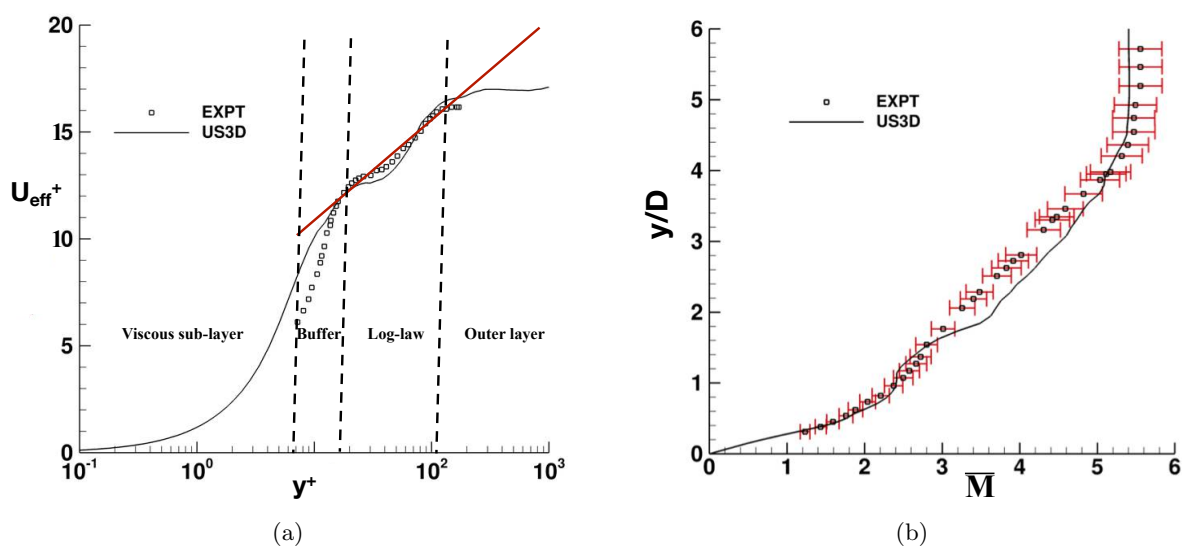


FIGURE 8: (a) van Driest mean velocity profile and (b) mean Mach number profile at $x/D = 86$.

the present section is truncated at $x/D = 100$. Furthermore, no freestream disturbance is imposed to more accurately isolate and analyze the flow physics.

A. UPSTREAM VORTEX SYSTEM

An extended one-vortex system is present upstream of the roughness element. Differences have been identified in the region between the present study and that of a low Reynolds number case (comparable to the present Reynolds number) of Subbareddy et al.⁶ We observe that the mean upstream extension of the recirculation is large due to the high blockage ratio (50%) in the present study. A higher blockage ratio means more flow accumulation upstream of the roughness elements and, therefore, a larger recirculation zone. Furthermore, more than one mean vortex is observed in Subbareddy et al.⁶ The mean recirculation region extends to 10D upstream as shown in Figure 9(a). The mean recirculation extension is almost spanwise constant. Figure 9(b) shows the top view of Q -criterion¹⁷ isosurfaces of the upstream vortex system. Q -criterion is the second invariant of the velocity gradient tensor and is a tool to identify vorticity. As per Figure 9(b), the vortex system wraps the trips locally near the wall region and form a pair of streamwise vortices downstream. Another pair of streamwise vortices originates from the wake region. Based on the Q -criterion isosurfaces, the vorticity of the streamwise vortices from the wake region is stronger. Furthermore, the vortex system is oscillatory in nature due to its breathing process. A 3-D video of the breathing process is shown in the link <https://youtu.be/NCu92oD4XWg>. The video contains isosurfaces of pressure colored by streamwise velocity. This breathing process may oscillate the perturbations observed in the downstream region of the trips as shown in the video.

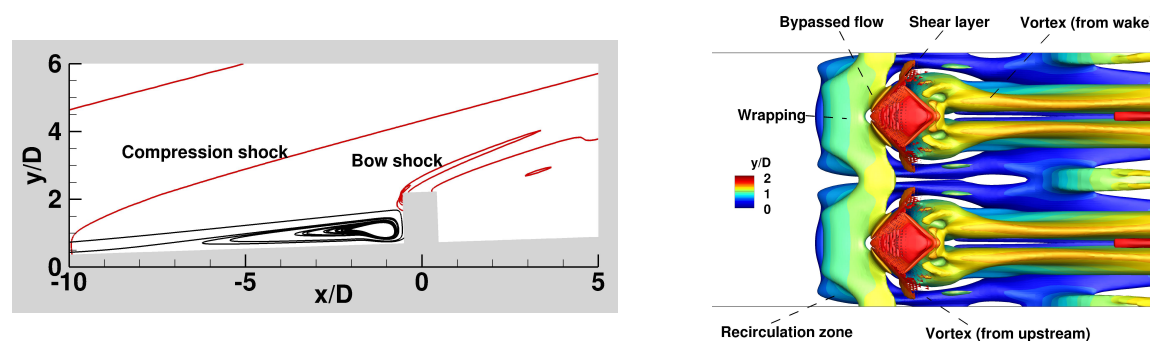


FIGURE 9: (a) Recirculation region upstream of the trips at $z/D = 1$ and (b) mean Q -criterion isosurfaces (colored by non-dimensionalized wall normal distance) near the trips (top view)

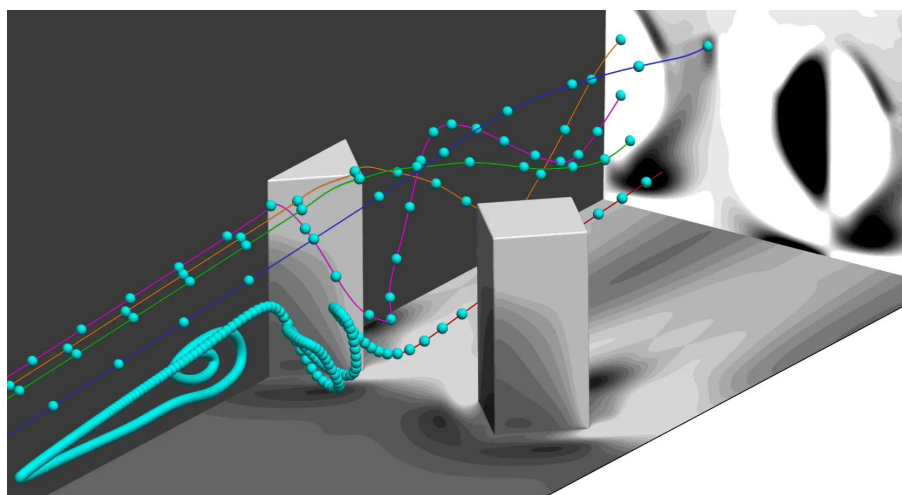


FIGURE 10: Mean trajectory of fluid particles. The wall and trips, and the streamwise plane on the right are contoured by total shear stresses and streamwise vorticity respectively. The symmetry plane on the left through the mid-trip section has no contour.

Figure 10 is to orient readers about trajectories of fluid particles using mean velocity streamtraces near the trips. The fluid particles, which form the upstream vortex system, wrap the roughness elements close to the wall and form a pair of streamwise vortices per trip. Since the mean velocity of the fluid particles is low in the upstream vortex system (close to the wall and the trip), the particles are heavily clustered along a streamtrace. However, since the mean velocity of the fluid particles, which travel on top of the vortex system, is higher, the fluid particles are less clustered along their streamtraces. Furthermore, the latter fluid particles wrap the trips around upper lateral regions of the trips to form a pair of streamwise vortices per trip from the wake regions. A formation of streamwise vortices is due to the fluid particles bouncing off the wall. The downstream motion of these particles is due to the pressure difference across the trips. This finding is consistent to the analysis performed using the Q -criterion isosurfaces in Figure 9(b). A video showing the motion of the fluid particles is in the link <https://www.youtube.com/watch?v=G3tpk6mV7U&feature=youtu.be>.

B. SEPARATED SHEAR LAYER/ COUNTER-ROTATING VORTEX SYSTEM

Flow traveling downstream on top of the upstream vortex system wraps the upper and top portion of the trips as shown in Figure 10. Two pairs of counter-rotating streamwise vortices per trip observed downstream at $x/D = 5$ are shown in Figure 11(a). The lower pairs of the vortical structures originate from the upstream vortex system while the upper pairs originate from the wake region. Downstream of the roughness elements, both the upper (from the wake region) and the lower (from the upstream vortex system) streamwise vortices uplift themselves away from the wall via “lift-up” mechanism.¹⁸ Since the lower pairs of vortices are close to the wall, they dissipate faster and become disoriented earlier. On top of the lower pairs of vortices, there is a constructive interference between the upper streamwise vortices and the 3-D shear layer formed from the top and sides of the trips. This interaction is shown by Figure 11(b). This then forms hairpin-like structures that indicate the onset of the transition process. The transition process is more clearly depicted by Figure 12.

Streamtraces of mean wall shear stresses on top of non-dimensionalized pressure contours are shown in Figure 13a and Figure 13(b). Both Figure 13(a) and Figure 13(b) represent the flow reversal and the origin of the streamwise vortices from the wake region from the back and the front views respectively. It is clearly observable that the flow from the upstream vortex system as well as the flow on top of the upstream vortex system form the origin of the upper streamwise vortices.

Moreover, the mean streamtraces are similar to those in the isolated cylinder case⁶ based on the topology of the streamtraces on the trip wall and the origin of the upper streamwise vortices. However, the streamtraces travel closer to the symmetry planes ($z/D = 1$ and $z/D = -1$) in the present study due to the higher blockage ratio.

C. SHOCK SYSTEM

The upstream vortex system is observed to oscillate and, therefore, the top upstream portions of the roughness elements, exposed to the post-shock hypersonic flow, form a bow shock. The flow on top of the upstream vortex system oscillates the stagnation region of the trips via a feedback mechanism (details are provided later in “power spectral density” section). The oscillation of the stagnation region moves the bow shock which then produces acoustic or pressure waves traveling downstream of the trips. Therefore, the shock system may take part in the transition process. In Figure 14, contours of mean total kinetic energy and root mean square values of pressure upstream of the trip are plotted at the symmetry plane $z/D = 1$. In Figure 14(a), strong prominence of root mean square of pressure indicates acoustics traveling upstream inside the recirculation zone. This pressure disturbances then perturb the incoming laminar boundary layer. The perturbed free-shear layer propagates downstream on top of the recirculation zone and later gets further perturbed locally by the upstream vortex core. This process leads to an oscillatory shock system producing the acoustic disturbances downstream.

D. FULL FLOW SYSTEM

In Figure 15, we present the overall image of the present case using the Q -criterion isosurfaces colored by non-dimensionalized streamwise velocity. The three regions of unsteadiness are clearly visible and, therefore, could play roles during transition in a coupled system. Thus, to understand this possible coupled mechanism in more details, spatio-temporal analysis is carried out in the next chapter.

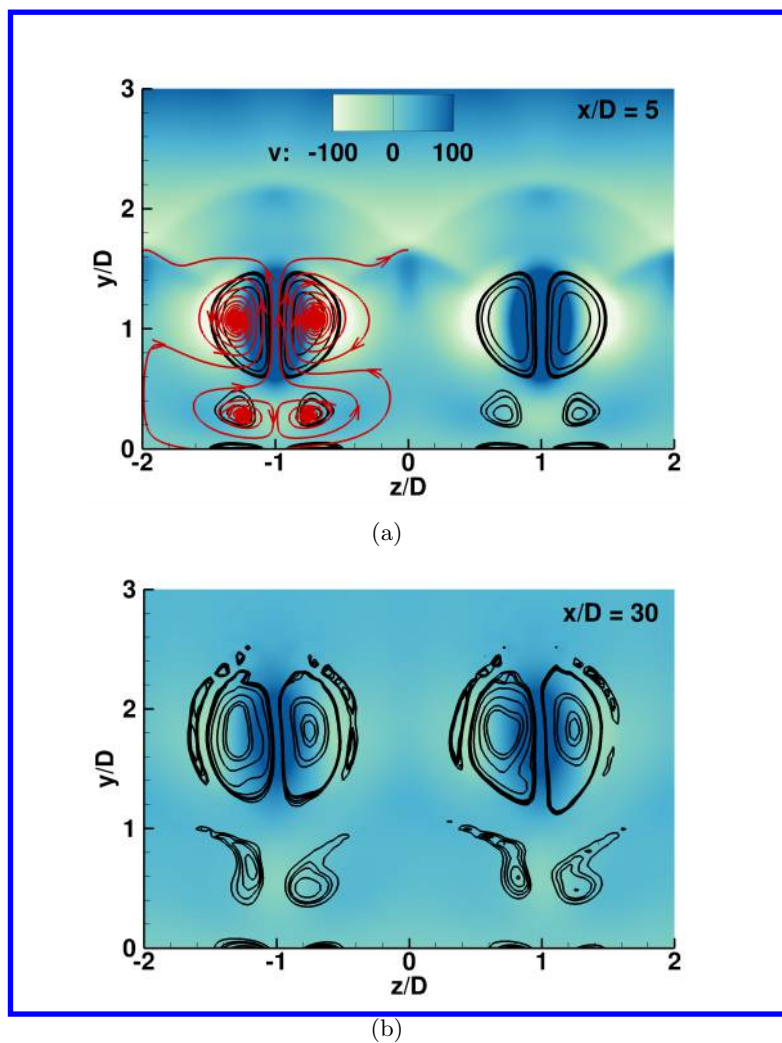


FIGURE 11: Mean wall normal velocity contours using mean velocity streamtraces to indicate flow directions of vortices (a) at $x/D = 5$ and (b) at $x/D = 30$. Line contours are of mean streamwise vorticity.

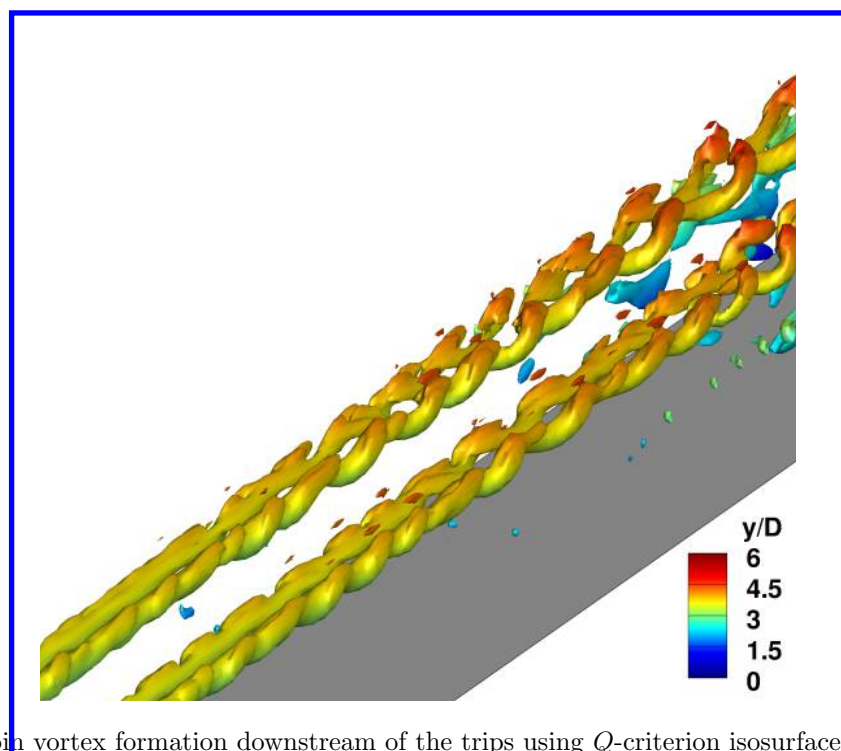


FIGURE 12: Hairpin vortex formation downstream of the trips using Q -criterion isosurfaces flooded by non-dimensionalized wall normal distance.

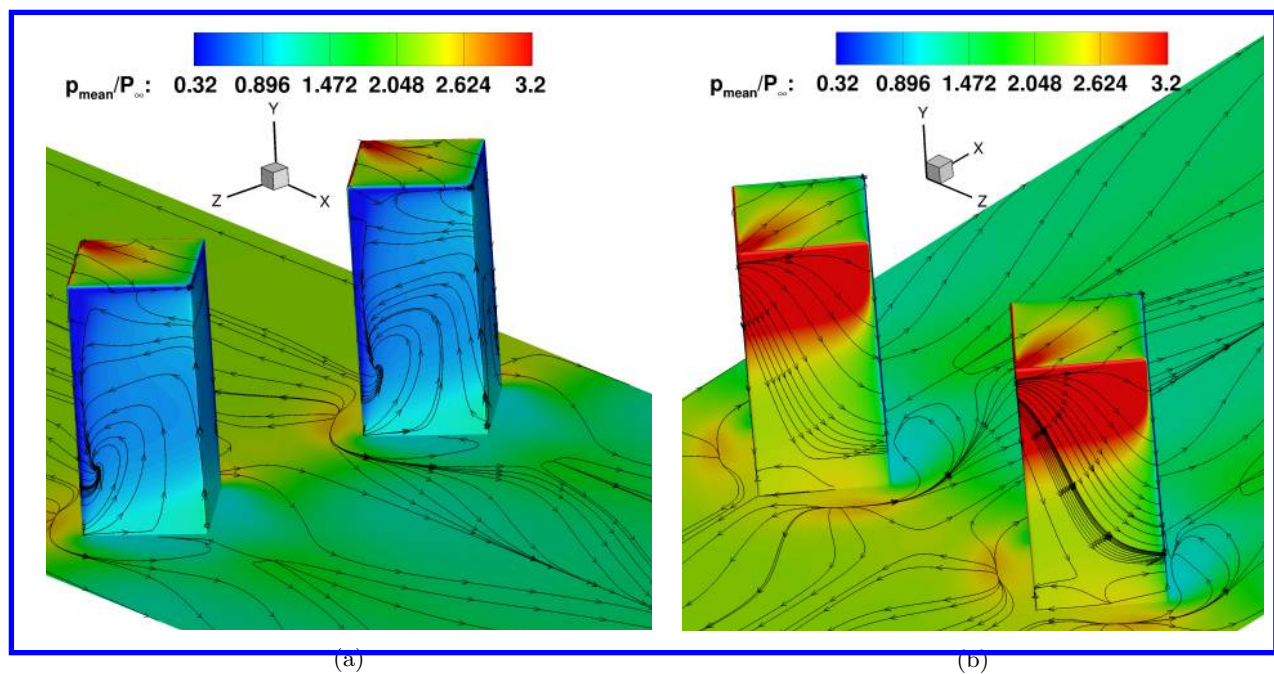


FIGURE 13: (a) Back and (b) front view of streamtraces of mean wall shear stresses around the roughness elements. Mean pressure contours are used.

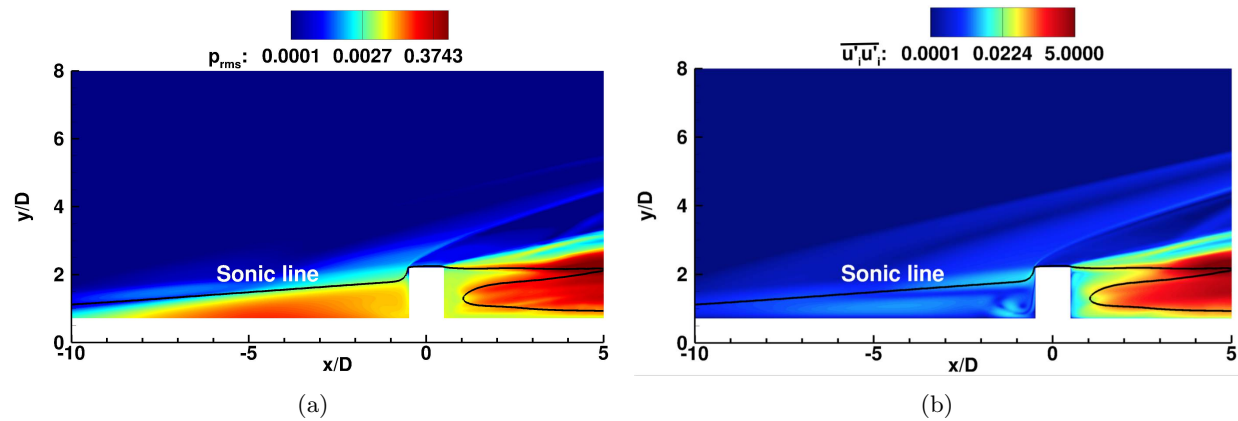


FIGURE 14: (a) Root mean square of pressure and (b) mean total kinetic energy (TKE) near the trip. $z/D = 1$

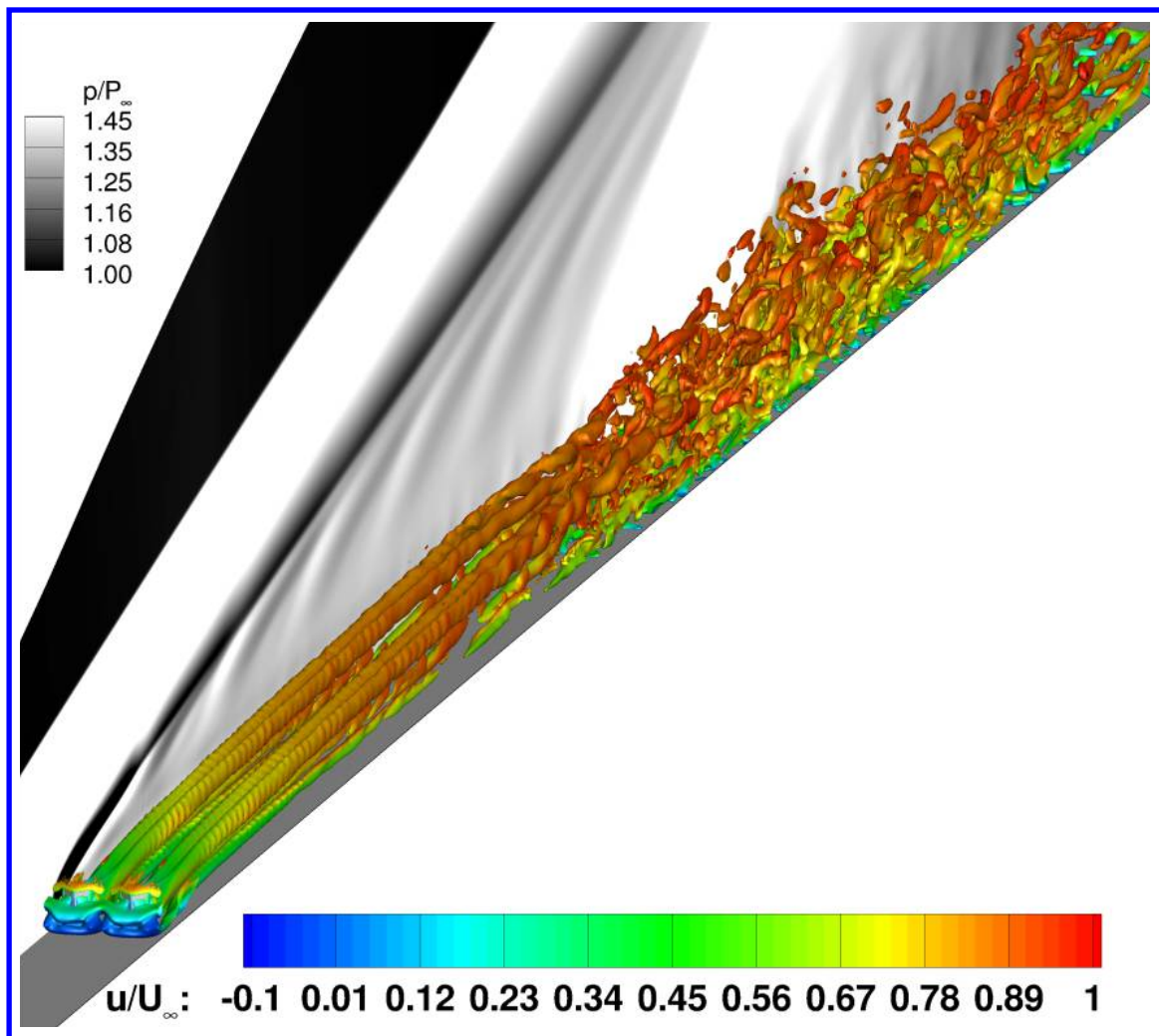


FIGURE 15: Q -criterion isosurfaces colored by the nondimensionalized streamwise velocity.

B. Spatio-temporal analysis

This section discusses FFT and DMD results of the present study to compare and understand contributions of different systems of unsteadiness during transition. Dynamic mode decomposition (DMD) is used to capture dominant and unsteady coherent structures, and understand their regions of origin and amplification. The DMD results are accompanied by the preceding FFT data at different relevant locations.

1. Power Spectral Density

The power spectral density of pressure fluctuations are analyzed at seven locations as shown in Figure 16. Figure 16 is contoured by pressure and instantaneous velocity streamtraces. The pressure contours are used to represent the shock system and the separated shear layer/wake region. The instantaneous velocity streamtraces depict the upstream vortex system. A sampling frequency is 5 MHz, the number of sampling is 8500 snapshots, and Hanning window is applied.

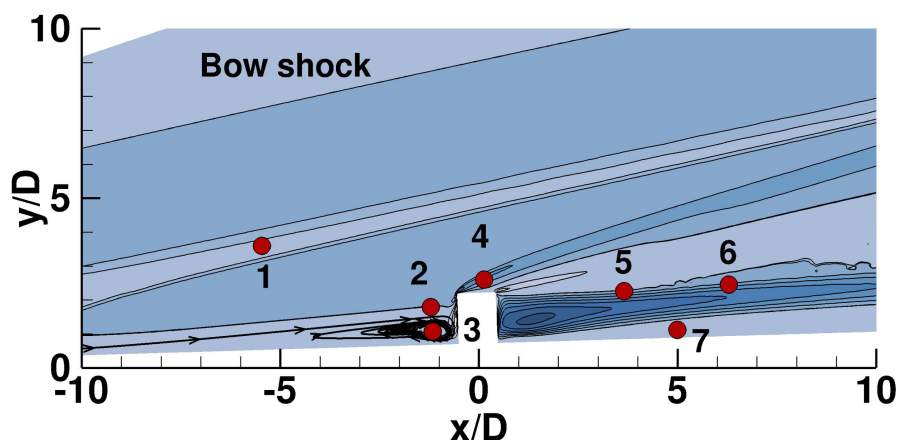


FIGURE 16: Probe locations for PSD calculations at $z/D = 1$.

In Figure 17(a), PSD plots at probe locations 1, 2, 3 and 4 are presented with respect to Strouhal number (St). Strouhal number is defined as $St = \frac{f \times D}{U_\infty}$, where f is frequency in Hz and U_∞ is the freestream streamwise velocity. Probe 1 lies in the upstream compression shock, probe 2 on top of the upstream vortex core, probe 3 inside the upstream vortex core and probe 4 behind the bow shock from the top and upstream portions of the roughness elements. A local peak at $St = 0.11$ corresponding to 30 kHz appears at all the probe locations. Since the PSD plots at all the probes are similar and the incoming boundary layer is laminar with no disturbance, the upstream vortex system appears to be the source of the local peak.

In Figure 17(b), PSD plots at probes 3, 5, 6 and 7 are presented with respect to St . Probes 5 and 6 lie in the region where the 3-D shear layer and the counter-rotating streamwise vortices interact with each other downstream of the roughness elements while probe 7 lies near the wall downstream close to counter-rotating streamwise vortices from the wake and the upstream vortex system. From Figure 17(b), the local peak observed in Figure 17(a) is highly amplified at these probe locations. Furthermore, there are its sub-harmonic frequencies with $St = 0.22$ and 0.33 . This suggests that the shear layer and the counter-rotating vortices from the wake region play a significant role in amplifying upstream signals. However, based on the PSD plot at the probe 7 location, the dominant region of amplification appears to be the wake region as the probe 7 is close to the streamwise counter-rotating vortices appearing from the wake region than to the 3-D shear layer.

2. Three-dimensional dynamic mode decomposition

Dynamic mode decomposition is a post-processing technique that utilizes a number of snapshots either from experiments or simulations. A snapshot means a realization of a flow variable within a domain of consideration at a time instant. DMD extracts eigenvalues and eigenvectors using a linear mapping from the n^{th} snapshot to the $(n + 1)^{th}$ snapshot. DMD and proper orthogonal decomposition (POD) work around

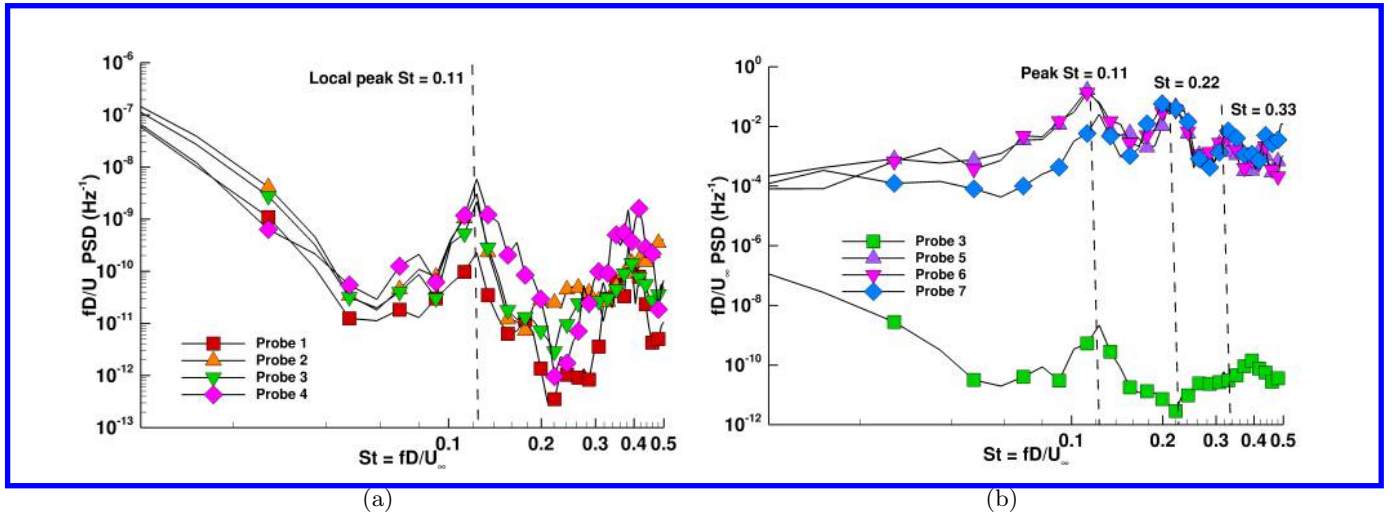


FIGURE 17: PSD plots at (a) upstream-shock system and (b) downstream system.

singular value decomposition (SVD). POD extracts modes that have broadband frequency content where as each DMD mode has its own frequency. However, DMD modes are non-orthogonal unlike POD modes. So, this lack of orthogonality of DMD modes makes it challenging to systematically identify a subset of modes that have the strongest impact on the flow dynamics. Jovanović et al.¹¹ addressed this problem by developing a sparsity promoting variant of the standard DMD algorithm. Sparsity-promoting dynamic mode decomposition (SPDMD) achieves a required adjustment between the quality of approximation and the number of DMD modes. The adjustment is carried out using the least-squares deviation (between the matrix of snapshots and the linear combination of selected DMD modes) with a supplementary term that penalizes the l_1 -norm of the vector of DMD amplitudes. For more information on DMD and SPDMD, readers are referred to Schmid,⁷ Boyd and Vandenberghe,¹⁹ Donoho,²⁰ Candes et al.²¹ and Jovanović et al.¹¹

Shrestha and Candler¹⁰ performed a two-dimensional SPDMD calculation on the wall using three roughness elements of the same $k/\delta = 1.48$ and $s/D = 2$. Qualitatively, DMD modes that originate from the upstream and the sides of the trips were observed to be dominant sources or modes of transition mechanisms. However, the region of snapshot included turbulent regions, and, therefore, the linear mapping between consecutive snapshots was not accurate using these snapshots. Therefore, in the present study, we apply DMD before the transition onset location. Moreover, the present study is three-dimensional and, therefore, a volumetric snapshot provides more detailed and accurate dynamics of the flow. In addition, a consideration of cell volumes around the trips is very important as each of these cells carry their own weight of information or they contribute to the flow dynamics based on their volume. For the selection of the most dominant modes, we implement Chu's norm.²² In DMD, snapshots of data are formed as columns into a matrix ψ (of size $M \times N$, say). M and N are total degrees of freedom and number of snapshots respectively. Using the method of snapshots, a set of POD modes P of size $M \times N$ is then computed. These modes satisfy $P^T H P = I$, where H defines the inner product. This inner product is chosen to be Chu's disturbance energy norm in our case as written below. For more information, readers are referred to Hanifi et al.²³ and Nichols et al.²⁴ In short, this norm applies the same sparsity processes as SPDMD but includes all the flow quantities.

$$H = \int_V \left\{ \frac{1}{2} \rho_o (u'^2 + v'^2 + w'^2) + \frac{1}{2} \frac{T_o \rho'^2}{\gamma \rho_o M^2} + \frac{1}{2} \frac{\rho_o T'^2}{\gamma (\gamma - 1) T_o M^2} \right\} dV \quad (10)$$

In (10), " X_o " means the time averaged value of variable " X ". All variables have usual meanings. The snapshot-field variable used in the present study is pressure so as to compare our modal structures with those of Subbareddy et al.⁶ Since the simulation is statistically stationary and the selecting norm is consistent, choosing any other field variables will not alter dominant modes.

The region of snapshot considered in the present study ranges as $x/D \in [-20, 30]$, $y/D \in [0, 9.5]$ and $z/D \in [-2, 2]$. Reasons to select this region are (1) the flow doesn't include flow breakdown regions (minimizes non-linearity), (2) all modes of transition can be studied and (3) the number of degrees of freedom is smaller (compared to the entire domain). The sampling time period is 2.5 μ sec and the number of snapshots is 100

in the present study. Since the frequency of the most unstable mode observed from the experiment is 58 kHz⁹ and the present Nyquist frequency is 100 kHz, the sampling frequency should be sufficient to capture relevant high frequency structures to study the transition mechanisms.

A. DMD RESULTS

$M = 40$ million cells and $N = 100$ snapshots. Using MPI FORTRAN based DMD code, Lapack/Blas packages, we compute and select relevant DMD modes based on Chu's norm. Since the ψ matrix is tall (M) and skinny (N), the TSQR algorithm²⁵ is implemented to carry out parallel QR factorizations. The algorithm²⁵ is very efficient and scalable for the present case.

A statistical convergence study of DMD amplitudes with respect to Strouhal number (based on U_∞ and D) is carried out and is shown in Figure 18(a). In Figure 18a, four analysis were performed with the interval frequency of 40 kHz. It is observed that the plots of DMD amplitudes converge as we change the first snapshot locations in real time. Furthermore, it is very interesting to observe three local peaks at $St = 0.11, 0.22$ and 0.28 . These local peaks correspond to the local peaks observed in Figure 17(b). Moreover, $N = 200$ snapshots produce similar plots with local peaks around the same Strouhal numbers.

The corresponding eigenvalue spectrum is shown in Figure 18(b).

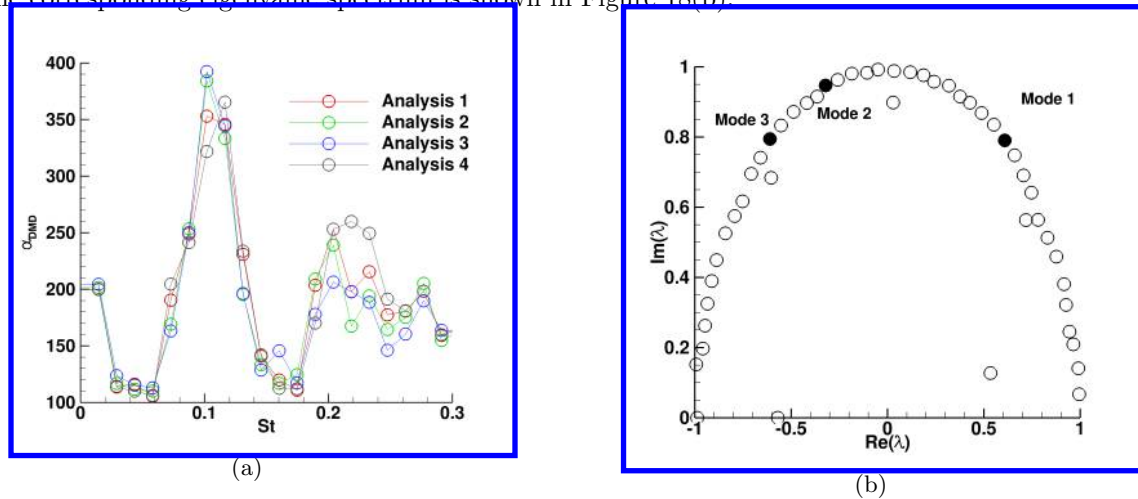


FIGURE 18: (a) DMD amplitudes vs. Strouhal number and (b) eigenvalue spectrum.

Three selected DMD modes are shown in Figure 18b with 30 kHz, 60 kHz and 70 kHz based on Chu's norm. Furthermore, performance loss is plotted in Figure 19a. Performance loss using a number of selected DMD modes is the deviation between the actual snapshot matrix ψ and a reconstructed matrix formed by the linear combination of the selected DMD modes. In Figure 19a, the first mode (30 kHz) retains almost 48% of the flow dynamics. The second mode (60 kHz) represents 18% of flow information while the third mode holds 8% of flow information. Likewise, sparsity-promoting parameter γ is varied to reduce dimensionality of the flow and retain significant DMD modes as shown in Figure 19b. For more information, readers are referred to Jovanović et al.¹¹

We discuss modal shapes of the three dominant modes as shown in Figure 20 and Figure 21. In Figure 20, a side view of the modes is presented. All modes are amplified as they travel downstream from the upstream vortex system to the wake/shear layer regions. Furthermore, the shock system is also observed to act as an amplifier. Based on the prominence of modal shapes and their intensity upstream and downstream of the roughness element in Figure 20, the mode 1 appears to be the most energetic mode with the upstream vortex system acting as the source of the dominant disturbance while the wake region is observed to be a dominant amplifier.

In Figure 21, the three modes are presented at the half-trip height and on a wall-parallel plane. Consistent with our previous findings, the first mode has the strongest spatial signature in the upstream region followed by the second and the third modes. All the modes are also observed to be amplified by the wake region of the roughness elements. Perturbations, that are observed in the wake region of the roughness elements, appear to travel downstream from the upstream vortex system. Hence, all the perturbations observed in the Q -criterion plot shown in Figure 15 originate from the upstream vortex system.

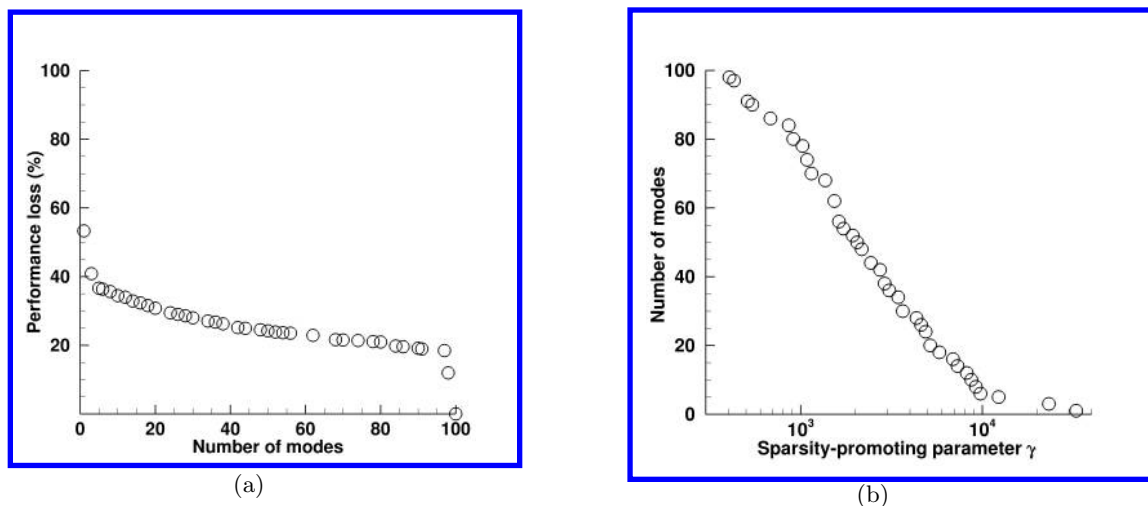


FIGURE 19: (a) Performance loss vs. number of modes retained and (b) number of modes retained vs. γ values.

A better illustration of this finding is shown in Figure 22 in which a streamwise evolution of the first DMD mode using different streamwise planes downstream of the roughness elements are present. In Figure 22, on the slice S1, strong modal shapes are observed near the wake region as compared to those in the separated shear layer region originating from the top of the roughness elements. Further downstream, on slices S2 and S3, the shear layer forms a 3-D wrapping on top of the streamwise vortices. Consistent to the DNS, these vortices are observed to lift-up away from the wall and interact with the 3-D shear layer. This interaction then leads to the formation of hairpin-like structures downstream that are an indication of the transition process. Similar plots and findings are observed in case of the second and the third DMD modes.

A video from the side view on the symmetry plane ($z/D = 1$) of the most dominant DMD mode can be played in the link <https://www.youtube.com/watch?v=XxulpCukIZw&feature=youtu.be>. In the video, it is observed that the breathing of the upstream vortex system sends acoustic disturbances away from its vortex core and perturbs the free-shear layer convecting on top of the recirculation zone. The perturbation appears to be dominantly absolute i.e. localized perturbations of the free-shear layer along the inflectional points. The perturbed free-shear layer forms the shock system, the separated shear layer, and the wake region all of which are amplified later.

DMD results by Subbareddy et al.⁶ were computed using smaller k/δ ($=1.23$) and higher Reynolds number (68000 based on roughness height and freestream velocity). Reynolds number in the present study is 24,000 which is much lower compared to previous work. However, qualitatively, we presume we can compare how the transition mechanisms in the array of trips differ from the isolated roughness element. In the isolated cylinder case, a horseshoe vortex system is observed as the most dominant mode of transition in terms of growth rate or amplitudes followed by the separated shear layer downstream of the trip. It is very important to note that the present study selects DMD modes based on Chu's norm as this norm incorporates all the flow quantities instead of using only pressure like in the previous work. Furthermore, similar shock system ahead of the roughness elements is observed consistently in all the modes.

B. SPATIAL EVOLUTION OF POWER SPECTRAL DENSITY

Spatial evolution of the PSD of pressure of 30 kHz, 60 kHz and 70 kHz DMD modes with respect to the streamwise distance at $z/D = 1$ and two y/D locations ($= 0.8$ and 1.5) are shown in Figure 23. $y/D = 0.8$ connects the upstream region and the wake region while $y/D = 1.5$ relates the upstream region and the shear layer/counter-rotating vortex region. This analysis is to correlate the PSD and the DMD results with spatial evolution of the frequency modes through the center of one of the trips. In Figure 23, spatial PSD plots at $y/D = 0.8$ show higher values compared to that at $y/D = 1.5$ just downstream of the roughness element. Furthermore, the spatial plots at the two y/D locations show considerable pressure amplitudes upstream of the trip. Thus, this finding suggests that the source of disturbance is the upstream vortex system while the most dominant source of amplification is the wake region.

The influence of the shock system and the shear layer is also observed as the PSD plots of all the frequency

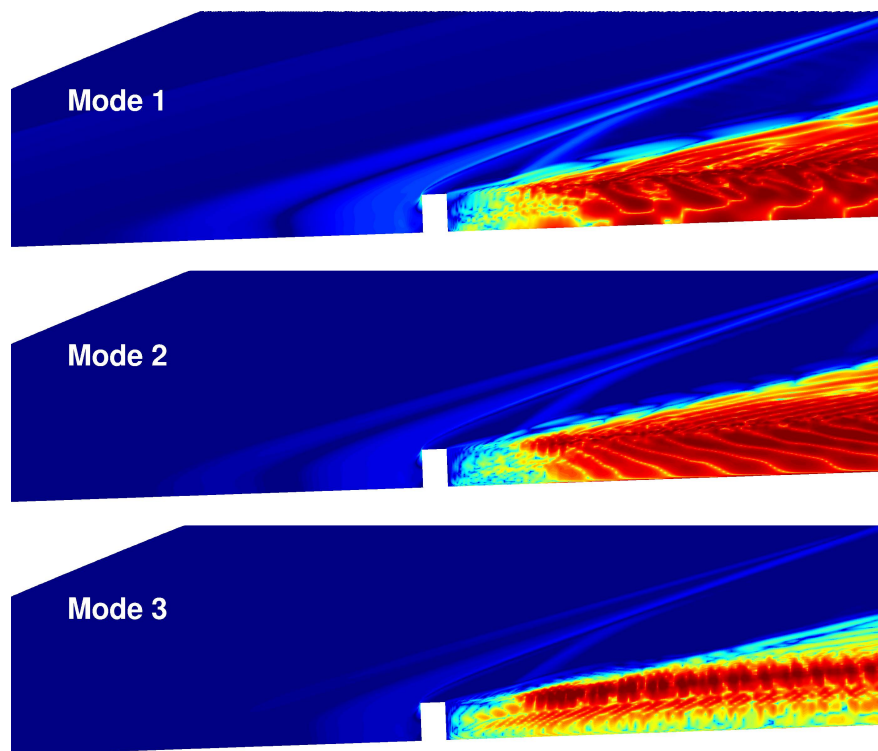


FIGURE 20: Modal shapes of all the three modes at $z/D = 1$ (symmetry plane).

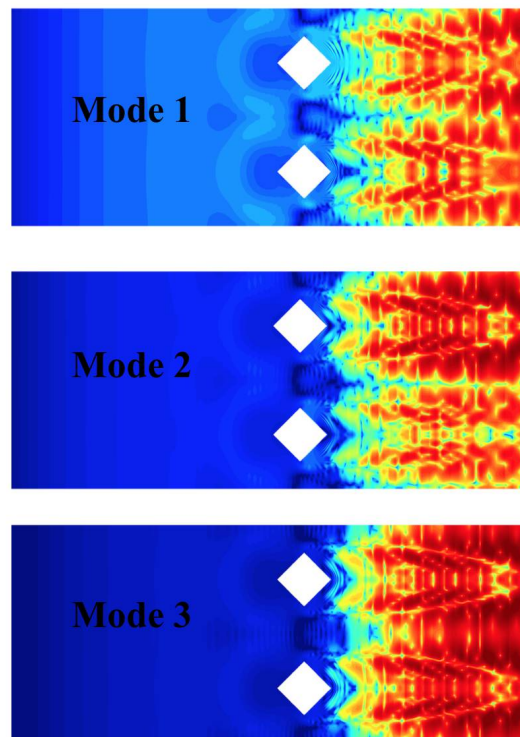


FIGURE 21: Modal shapes of all the three modes at $y/D = 0.8$.

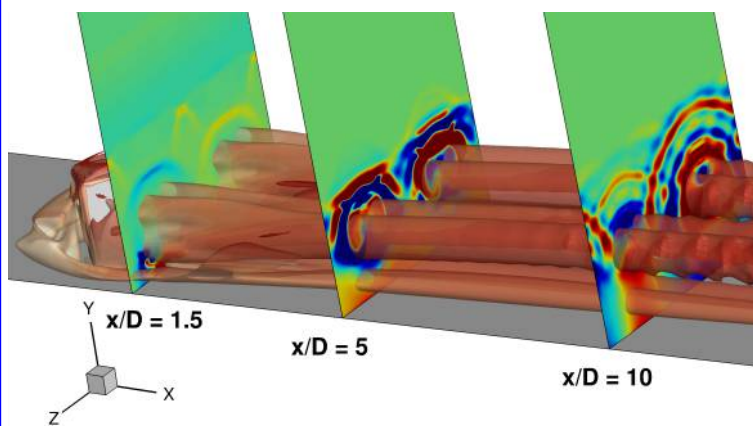


FIGURE 22: Streamwise evolution of the first DMD mode downstream of the roughness elements.

modes at $y/D = 1.5$ is higher than those at $y/D = 0.8$ after $x/D = 8$. So, at around the trip height along the streamwise direction, downstream traveling acoustics/separated shear layer modes appear to form a constructive interference with streamwise vortices from the wake region to cause transition.

Moreover, the PSD plots of the dominant DMD mode (30 kHz) have higher values mostly in all locations than those of the other two modes. This finding is consistent with the DMD and the previous PSD analysis.

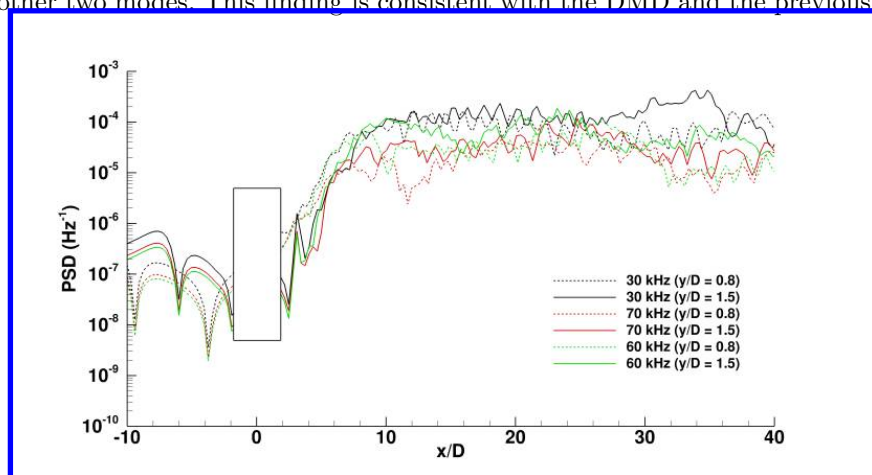


FIGURE 23: Spatial evolution of PSD of pressure of 30, 60 and 70 kHz frequencies at $z/D = 1$.

IV. Conclusion and future work

Direct numerical simulation is used to study transition of an initially laminar hypersonic boundary layer due to the presence of a spanwise array of diamond shaped roughness elements. The current study is based on a low Reynolds number hypersonic flow experiment that was carried out at the ACE facility, Texas A & M University. The value of k/δ is 1.48 (tall roughness elements) and s/D is 2 (50% blockage ratio). Three prominent regions of unsteadiness are observed : (1) the upstream vortex system, (2) the separated shear layer/counter-rotating vortex system, and (3) the shock system. There is only one mean vortex core observed in the present study and the extended recirculation zone upstream of the roughness elements due to the high blockage ratio. Furthermore, flow trajectory analysis indicates that flow wraps around the elements much closer to the plane ($z/D=1$) parallel to the streamwise direction. The origin of dominant disturbances is observed to be the upstream vortex system whereas the wake, the shock system, and the separated shear layer region act as amplifiers. More specifically, the wake region is observed to play the most dominant role

in transition to turbulence processes as suggested by PSD, flowfield analysis, and DMD.

The Dominant disturbances are primarily generated in the upstream vortex region due to its breathing process. The disturbances from the vortex core travel upstream as acoustics and perturb the free-shear layer formed in the upstream region of the vortex system. The perturbed free-shear layer is further disturbed near the roughness element due to vortical disturbances originating from the upstream vortex core. The perturbations are then carried downstream on top of the upstream vortex system. These perturbations travel into the three important regions. Unlike the isolated cylinder case,⁶ the shock system oscillates due to the perturbations interacting with the bow shock and not with the compression shock. It is observed that the wake region and the 3-D shear layer amplify the disturbances in which a constructive interference between the 3-D shear layer and the counter-rotating streamwise vortices appearing from the wake region leads to the formation of hair-pin like structures. These structures then dissipate their energy leading to turbulence downstream.

In summary, the transition mechanism in the present study is the coupled system in which the source of dominant disturbance is the upstream vortex system while the most dominant amplifier appears to be the wake region. Future work includes an investigation of instability mechanisms using different Reynolds numbers, Mach numbers, and trip configurations will enhance our understanding of this physical mechanism in a broader sense. Global stability and adjoint analysis of a base flow of the current trip configuration could provide more insights in the present findings. It will also serve as a verification of the most dominant DMD mode and the region of maximum sensitivity which is the wake region.

The regions of unsteadiness were initially reported in a AIAA conference paper by Shrestha and Candler.¹⁰ Flow visualizations exhibit the upstream vortex system, the shear layer/counter-rotating vortex system and the shock system in details. Power spectral density and dynamic mode decomposition are found to be effective tools to determine the origin of disturbances and the regions of their amplification.

Acknowledgment

The authors gratefully acknowledge the Office of Naval Research through grant number N00014-15-1-2522 for the support of this research. The suggestions and findings obtained herein are those of the authors and should not be interpreted as necessarily representing the official policies or endorsements, either expressed or implied, of the Office of Naval Research. The authors thank Michael Semper and Rodney Bowersox for providing experimental data to validate the present study.

Références

- ¹Tani, I., Komoda, H. and Komatsu, Y., “Boundary-layer transition by isolated roughness”, Tech. Rep. 375. Aeronautical Research Institute, University of Tokyo, 1962.
- ²Whitehead, Jr., A. H., “Flow-field and drag characteristics of several boundary layer tripping elements in hypersonic flow”, NASA Technical Report, Washington, D.C., 1969.
- ³Balakumar, P. and Kegerise, M., “Roughness Induced Transition in a Supersonic Boundary Layer”, 43rd AIAA Fluid Dynamics Conference, June 24-27, 2013, San Diego, California.
- ⁴Choudhari, M., Li, F., Wu, M., Chang C., Edwards, J., Kegerise, M. and King, R., “Laminar-Turbulent Transition behind Discrete Roughness Elements in a High-Speed Boundary Layer”, 48th AIAA, 4-7 January 2010, Orlando, Florida.
- ⁵Borg, M. P., Schneider, S. P. and Julian, T. J., “Effect Of Freestream Noise on Roughness-Induced Transition for the X-51A Forebody”, AIAA Paper 2008-0592, 2008.
- ⁶Subbareddy, P. K., Bartkiewicz, M. D. and Candler, G. V., “Direct numerical simulation of high-speed transition due to an isolated roughness element”, Journal of Fluid Mechanics, Volume 748, June 2014, pp. 848-878.
- ⁷Schmid, P. J., “Dynamic mode decomposition of numerical and experimental data”, Journal of Fluid Mechanics, Volume 656, pp 5- 28, August 2010.
- ⁸Berry, S. A., Auslender, A. H., Dilley, A. D. and Calleja, J. F., “Hypersonic Boundary Layer Trip Development for Hyper-X”, Journal of Spacecraft and Rockets, Vol. 38, No. 6, pp. 853-864, 2001.
- ⁹Semper, M. T. Bowersox, R., “Tripping of a Hypersonic Low-Reynolds-Number Boundary Layer”, AIAA Journal, Vol. 55, No. 3 (2017), pp. 808-817.
- ¹⁰Shrestha, P. and Candler, G. V., “Direct Numerical Simulation of Trip Induced Transition”, 46th AIAA Fluid Dynamics Conference, AIAA Aviation, (AIAA 2016-4380).
- ¹¹Jovanovic, M. R., Schmid, P. J. and Nichols, J. W., “Sparsity-promoting dynamic mode decomposition”, Physics of Fluids, 26, 024103, 2014.
- ¹²Laufer, J., “Aerodynamics Noise in Supersonic Wind Tunnels”, Journal of the Aerospace Sciences, Vol. 28, pp. 685-692, September 192.
- ¹³Subbareddy, P. K. and Candler, G. V., “A fully discrete, kinetic energy consistent finite-volume scheme for compressible flows”, Journal of Computational Physics, Vol. 228, No. 5, pp. 1347-1364, 2009.
- ¹⁴Ducros, F., Ferrand, V., Nicoud, F., Weber, C., Darracq, D., Gacherieu, C., and Poinot, T., “Large-Eddy Simulation of the Shock/Turbulence Interaction”, Journal of Computational Physics, Vol.152, No. 2, pp. 517 - 549, 1999.

- ¹⁵Wright, M. J., Candler, G. V. and Bose, D., “*Data-Parallel Line Relaxation Method for the NavierStokes Equations*”, AIAA Journal, Vol. 36, No. 9, September 1998.
- ¹⁶van Driest, E., “*On turbulent flow near a wall*”, J. Aeronaut. Sci. 23 (11), 10071011, 1956.
- ¹⁷Dubief, Y. and Delcayre, F., “*On coherent-vortex identification in turbulence*”, Journal of Turbulence, 1, N11, January 2001.
- ¹⁸Brandt, L., “*The lift-up effect : the linear mechanism behind transition and turbulence in shear flows*”, Elsevier, 2014.
- ¹⁹Boyd, S. and Vandenberghe, L., “*Convex optimization*”, Cambridge University Press, New York, 2004.
- ²⁰Donoho, D. L., “*Compressed sensing*”, IEEE Transactions on Information Theory, Vol. 52, No. 4, pp. 1289-1306, 2006.
- ²¹Candes, E. J., Wakin, M. B. and Boyd, S. P., L., “*Enhancing sparsity by reweighted 1 minimization*”, Journal of Fourier Analysis Applications, Vol. 14, pp. 877-905, 2008.
- ²²Chu, B.-T., “*On the energy transfer to small disturbances in fluid flow (part i)*”, Acta Mechanica 1, 215234, 1965.
- ²³Hanifi, A., Schmid, P. J. and Henningson, D. S., “*Transient growth in compressible boundary layer flow*”, Physics of Fluids (1994-present) 8, 826 (1996).
- ²⁴Nichols, J. W., Larsson, J. and Bernardini, M., “*Stability and modal analysis of shock/boundary layer interactions*”, Theor. Comput. Fluid Dyn. (2017) 31 :3350.
- ²⁵Sayadi, T. and Schmid, P. J., “*Parallel data-driven decomposition algorithm for large-scale datasets : with application to transitional boundary layers*”, Theor. Comput. Fluid Dyn. (2016) 30 :415428.